Measurement of the atmospheric muon spectrum from 20 to 3000 GeV

L3 Collaboration

P. Achard [v], O. Adriani [s], M. Aguilar-Benitez [aa], M. van den Akker [ag], J. Alcaraz [aa], G. Alemanni [y], J. Allaby [t], A. Aloisio [ae], M.G. Alviggi [ae], H. Anderhub [ba], V.P. Andreev [f,ak], F. Anselmo [j], A. Arefiev [ad], T. Azemoon [c], T. Aziz [k], P. Bagnaia [ap], A. Bajo [aa], G. Baksay [ab], L. Baksay [ab], J. Bähr [az], S.V. Baldew [b], S. Banerjee [k], Sw. Banerjee [d], A. Barczyk [ba,ay], R. Barillère [t], P. Bartalini [y], M. Basile [j], N. Batalova [ax], R. Battiston [aj], A. Bay [y], F. Becattini [s], U. Becker [o], F. Behner [ba], L. Bellucci [s], R. Berbeco [c], J. Berdugo [aa], P. Berges [o], B. Bertucci [aj], B.L. Betev [ba], M. Biasini [aj], M. Biglietti [ae], A. Biland [ba], J.J. Blaising [d], S.C. Blyth [al], G.J. Bobbink [b], A. Böhm [a], L. Boldizsar [n], B. Borgia [ap], S. Bottai [s], D. Bourilkov [ba], M. Bourquin [v], S. Braccini [v], J.G. Branson [ar], F. Brochu [d], J.D. Burger [o], W.J. Burger [aj], X.D. Cai [o], M. Capell [o], G. Cara Romeo [j], G. Carlino [ae], A. Cartacci [s], J. Casaus [aa], F. Cavallari [ap], N. Cavallo [am], C. Cecchi [aj], M. Cerrada [aa], M. Chamizo [v], T. Chiarusi [s], Y.H. Chang [av], M. Chemarin [z], A. Chen [av], G. Chen [g], G.M. Chen [g], H.F. Chen [x], H.S. Chen [g], G. Chiefari [ae], L. Cifarelli [aq], F. Cindolo [j], I. Clare [o], R. Clare [ao], G. Coignet [d], N. Colino [aa], S. Costantini [ap], B. de la Cruz [aa], S. Cucciarelli [aj], J.A. van Dalen [ag], R. de Asmundis [ae], P. Déglon [v], J. Debreczeni [n], A. Degré [d], K. Dehmelt [ab], K. Deiters [ay], D. della Volpe [ae], E. Delmeire [v], P. Denes [an], F. DeNotaristefani [ap], A. De Salvo [ba], M. Diemoz [ap], M. Dierckxsens [b], L.K. Ding [g], C. Dionisi [ap], M. Dittmar [ba], A. Doria [ae], M.T. Dova [l,5], D. Duchesneau [d], M. Duda [a], I. Duran [as], B. Echenard [v], A. Eline [t], A. El Hage [a], H. El Mamouni [z], A. Engler [al], F.J. Eppling [o], P. Extermann [v], G. Faber [ba], M.A. Falagan [aa], S. Falciano [ap], A. Favara [ai], J. Fay [z], O. Fedin [ak], M. Felcini [ba], T. Ferguson [al], H. Fesefeldt [a], E. Fiandrini [aj], J.H. Field [v], F. Filthaut [ag], W. Fisher [an], I. Fisk [ar], G. Forconi [o], K. Freudenreich [ba], C. Furetta [ac], Yu. Galaktionov [ad,o], S.N. Ganguli [k], P. Garcia-Abia [aa], M. Gataullin [ai], S. Gentile [ap], S. Giagu [ap], Z.F. Gong [x], H.J. Grabosch [az], G. Grenier [z], O. Grimm [ba], H. Groenstege [b], M.W. Gruenewald [r], M. Guida [aq], Y.N. Guo [g], S. Gupta [k], V.K. Gupta [an], A. Gurtu [k], L.J. Gutay [ax], D. Haas [e],

Ch. Haller [ba], D. Hatzifotiadou [j], Y. Hayashi [ah], Z.X. He [h], T. Hebbeker [a], A. Hervé [t], J. Hirschfelder [al], H. Hofer [ba], H. Hofer Jr. [ba], M. Hohlmann [ab], G. Holzner [ba], S.R. Hou [av], A.X. Huo [g], Y. Hu [ag], N. Ito [ah], B.N. Jin [g], C.L. Jing [g], L.W. Jones [c], P. de Jong [b], I. Josa-Mutuberría [aa], V. Kantserov [az,7], M. Kaur [p], S. Kawakami [ah], M.N. Kienzle-Focacci [v], J.K. Kim [au], J. Kirkby [t], W. Kittel [ag], A. Klimentov [o,ad], A.C. König [ag], E. Kok [b], A. Korn [o], M. Kopal [ax], V. Koutsenko [o,ad], M. Kräber [ba], H.H. Kuang [g], R.W. Kraemer [al], A. Krüger [az], J. Kuijpers [ag], A. Kunin [o], P. Ladron de Guevara [aa], I. Laktineh [z], G. Landi [s], M. Lebeau [t], A. Lebedev [o], P. Lebrun [z], P. Lecomte [ba], P. Lecoq [t], P. Le Coultre [ba], J.M. Le Goff [t], Y. Lei [g], H. Leich [az], R. Leiste [az], M. Levtchenko [ac], P. Levtchenko [ak], C. Li [x], L. Li [g], Z.C. Li [g], S. Likhoded [az], C.H. Lin [av], W.T. Lin [av], F.L. Linde [b], L. Lista [ae], Z.A. Liu [g], W. Lohmann [az], E. Longo [ap], Y.S. Lu [g], C. Luci [ap], L. Luminari [ap], W. Lustermann [ba], W.G. Ma [x], X.H. Ma [g], Y.Q. Ma [g], L. Malgeri [v], A. Malinin [ad], C. Maña [aa], J. Mans [an], J.P. Martin [z], F. Marzano [ap], K. Mazumdar [k], R.R. McNeil [f], S. Mele [t,ae], X.W. Meng [g], L. Merola [ae], M. Meschini [s], W.J. Metzger [ag], A. Mihul [m], A. van Mil [ag], H. Milcent [t], G. Mirabelli [ap], J. Mnich [a], G.B. Mohanty [k], B. Monteleoni [s,✠], G.S. Muanza [z], A.J.M. Muijs [b], B. Musicar [ar], M. Musy [ap], S. Nagy [q], R. Nahnhauer [az], V.A. Naumov [s,8], S. Natale [v], M. Napolitano [ae], F. Nessi-Tedaldi [ba], H. Newman [ai], A. Nisati [ap], T. Novak [ag], H. Nowak [az], R. Ofierzynski [ba], G. Organtini [ap], I. Pal [ax], C. Palomares [aa], P. Paolucci [ae], R. Paramatti [ap], J.-F. Parriaud [z], G. Passaleva [s], S. Patricelli [ae], T. Paul [l], M. Pauluzzi [aj], C. Paus [o], F. Pauss [ba], M. Pedace [ap], S. Pensotti [ac], D. Perret-Gallix [d], B. Petersen [ag], D. Piccolo [ae], F. Pierella [j], M. Pieri [s], M. Pioppi [aj], P.A. Piroué [an], E. Pistolesi [ac], V. Plyaskin [ad], M. Pohl [v], V. Pojidaev [s], J. Pothier [t], D. Prokofiev [ak], J. Quartieri [aq], C.R. Qing [h], G. Rahal-Callot [ba], M.A. Rahaman [k], P. Raics [q], N. Raja [k], R. Ramelli [ba], P.G. Rancoita [ac], R. Ranieri [s], A. Raspereza [az], K.C. Ravindran [k], P. Razis [af], D. Ren [ba], M. Rescigno [ap], S. Reucroft [l], P. Rewiersma [b,✠], S. Riemann [az], K. Riles [c], B.P. Roe [c], A. Rojkov [ba,ag,s], L. Romero [aa], A. Rosca [az], C. Rosemann [a], C. Rosenbleck [a], S. Rosier-Lees [d], S. Roth [a], J.A. Rubio [t], G. Ruggiero [s], H. Rykaczewski [ba], R. Saidi [i], A. Sakharov [ba], S. Saremi [f], S. Sarkar [ap], J. Salicio [t], E. Sanchez [aa], C. Schäfer [t], V. Schegelsky [ak], V. Schmitt [i], B. Schoeneich [az], H. Schopper [w], D.J. Schotanus [ag], C. Sciacca [ae], L. Servoli [aj], C.Q. Shen [g], S. Shevchenko [ai], N. Shivarov [at], V. Shoutko [o], E. Shumilov [ad], A. Shvorob [ai], D. Son [au], C. Souga [z], P. Spillantini [s], M. Steuer [o], D.P. Stickland [an], B. Stoyanov [at], A. Straessner [v], K. Sudhakar [k], H. Sulanke [az], G. Sultanov [at], L.Z. Sun [x], S. Sushkov [a], H. Suter [ba], J.D. Swain [l], Z. Szillasi [ab,3], X.W. Tang [g], P. Tarjan [q], L. Tauscher [e], L. Taylor [l], B. Tellili [z], D. Teyssier [z], C. Timmermans [ag], Samuel C.C. Ting [o], S.M. Ting [o], S.C. Tonwar [k], J. Tóth [n], G. Trowitzsch [az], C. Tully [an], K.L. Tung [g], J. Ulbricht [ba], M. Unger [az], E. Valente [ap], H. Verkooijen [b], R.T. van de Walle [ag], R. Vasquez [ax], V. Veszpremi [ab], G. Vesztergombi [n],

I. Vetlitsky [ad], D. Vicinanza [aq], G. Viertel [ba], S. Villa [ao], M. Vivargent [d], S. Vlachos [e],
I. Vodopianov [ab], H. Vogel [al], H. Vogt [az], I. Vorobiev [al,ad], A.A. Vorobyov [ak],
M. Wadhwa [e], R.G. Wang [g], Q. Wang [ag], X.L. Wang [x], X.W. Wang [g], Z.M. Wang [x],
M. Weber [t], R. van Wijk [b], T.A.M. Wijnen [ag], H. Wilkens [ag], S. Wynhoff [an], L. Xia [ai],
Y.P. Xu [ba], J.S. Xu [g], Z.Z. Xu [x], J. Yamamoto [c], B.Z. Yang [x], C.G. Yang [g], H.J. Yang [c],
M. Yang [g], X.F. Yang [g], Z.G. Yao [ba], S.C. Yeh [aw], Z.Q. Yu [g], An. Zalite [ak], Yu. Zalite [ak],
C. Zhang [g], F. Zhang [g], J. Zhang [g], S. Zhang [g], Z.P. Zhang [x], J. Zhao [x], S.J. Zhou [g],
G.Y. Zhu [g], R.Y. Zhu [ai], H.L. Zhuang [g], Q.Q. Zhu [g], A. Zichichi [j,t,u], B. Zimmermann [ba],
M. Zöller [a], A.N.M. Zwart [b]

[a] *III. Physikalisches Institut, RWTH, D-52056 Aachen, Germany* [1]
[b] *National Institute for High Energy Physics, NIKHEF, and University of Amsterdam, NL-1009 DB Amsterdam, The Netherlands*
[c] *University of Michigan, Ann Arbor, MI 48109, USA*
[d] *Laboratoire d'Annecy-le-Vieux de Physique des Particules, LAPP, IN2P3-CNRS, BP 110, F-74941 Annecy-le-Vieux cedex, France*
[e] *Institute of Physics, University of Basel, CH-4056 Basel, Switzerland*
[f] *Louisiana State University, Baton Rouge, LA 70803, USA*
[g] *Institute of High Energy Physics, IHEP, 100039 Beijing, China* [6]
[h] *ITP, Academia Sinica, 100039 Beijing, China*
[i] *Humboldt University, D-10115 Berlin, Germany*
[j] *University of Bologna and INFN Sezione di Bologna, I-40126 Bologna, Italy*
[k] *Tata Institute of Fundamental Research, Mumbai (Bombay) 400 005, India*
[l] *Northeastern University, Boston, MA 02115, USA*
[m] *Institute of Atomic Physics and University of Bucharest, R-76900 Bucharest, Romania*
[n] *Central Research Institute for Physics of the Hungarian Academy of Sciences, H-1525 Budapest 114, Hungary* [2]
[o] *Massachusetts Institute of Technology, Cambridge, MA 02139, USA*
[p] *Panjab University, Chandigarh 160 014, India*
[q] *KLTE-ATOMKI, H-4010 Debrecen, Hungary* [3]
[r] *Department of Experimental Physics, University College Dublin, Belfield, Dublin 4, Ireland*
[s] *University of Florence and INFN, Sezione di Firenze, I-50019 Sesto Fiorentino, Italy*
[t] *European Laboratory for Particle Physics, CERN, CH-1211 Geneva 23, Switzerland*
[u] *World Laboratory, FBLJA Project, CH-1211 Geneva 23, Switzerland*
[v] *University of Geneva, CH-1211 Geneva 4, Switzerland*
[w] *University of Hamburg, D-22761 Hamburg, Germany*
[x] *Chinese University of Science and Technology, USTC, Hefei, Anhui 230 029, China* [6]
[y] *University of Lausanne, CH-1015 Lausanne, Switzerland*
[z] *Institut de Physique Nucléaire de Lyon, IN2P3-CNRS, Université Claude Bernard, F-69622 Villeurbanne, France*
[aa] *Centro de Investigaciones Energéticas, Medioambientales y Tecnológicas, CIEMAT, E-28040 Madrid, Spain* [4]
[ab] *Florida Institute of Technology, Melbourne, FL 32901, USA*
[ac] *INFN Sezione di Milano, I-20133 Milan, Italy*
[ad] *Institute of Theoretical and Experimental Physics, ITEP, Moscow, Russia*
[ae] *INFN Sezione di Napoli and University of Naples, I-80125 Naples, Italy*
[af] *Department of Physics, University of Cyprus, Nicosia, Cyprus*
[ag] *University of Nijmegen and NIKHEF, NL-6525 ED Nijmegen, The Netherlands*
[ah] *Osaka City University, Osaka 558-8585, Japan*
[ai] *California Institute of Technology, Pasadena, CA 91125, USA*
[aj] *INFN Sezione di Perugia and Università Degli Studi di Perugia, I-06100 Perugia, Italy*
[ak] *Nuclear Physics Institute, St. Petersburg, Russia*
[al] *Carnegie Mellon University, Pittsburgh, PA 15213, USA*
[am] *INFN Sezione di Napoli and University of Potenza, I-85100 Potenza, Italy*
[an] *Princeton University, Princeton, NJ 08544, USA*
[ao] *University of California, Riverside, CA 92521, USA*
[ap] *INFN Sezione di Roma and University of Rome, "La Sapienza", I-00185 Rome, Italy*

[aq] *University and INFN, Salerno, I-84100 Salerno, Italy*
[ar] *University of California, San Diego, CA 92093, USA*
[as] *University of Santiago de Compostela, E-15706 Santiago, Spain*
[at] *Bulgarian Academy of Sciences, Central Laboratory of Mechatronics and Instrumentation, BU-1113 Sofia, Bulgaria*
[au] *The Center for High Energy Physics, Kyungpook National University, 702-701 Taegu, Republic of Korea*
[av] *National Central University, Chung-Li, Taiwan, ROC*
[aw] *Department of Physics, National Tsing Hua University, Taiwan, ROC*
[ax] *Purdue University, West Lafayette, IN 47907, USA*
[ay] *Paul Scherrer Institut, PSI, CH-5232 Villigen, Switzerland*
[az] *DESY, D-15738 Zeuthen, Germany*
[ba] *Eidgenössische Technische Hochschule, ETH Zürich, CH-8093 Zürich, Switzerland*

The L3 + C group dedicates this publication to the late Bianca Monteleoni

Abstract

The absolute muon flux between 20 and 3000 GeV is measured with the L3 magnetic muon spectrometer for zenith angles ranging from $0°$ to $58°$. Due to the large exposure of about 150 m^2 sr d, and the excellent momentum resolution of the L3 muon chambers, a precision of 2.3% at 150 GeV in the vertical direction is achieved.

The ratio of positive to negative muons is studied between 20 and 500 GeV, and the average vertical muon charge ratio is found to be $1.285 \pm 0.003(\text{stat.}) \pm 0.019(\text{syst.})$.

1. Introduction

Atmospheric muons are among the final products of cosmic ray induced air-showers. The absolute muon flux and its momentum dependence are mainly deter-

mined by the flux of nucleons entering the atmosphere and the inclusive meson production cross sections in high-energy hadronic interactions. The ratio of the fluxes of positive to negative muons, denoted as charge ratio in the following, reflects the proton to neutron ratio at the top of the atmosphere, folded with the production and decay spectra of charged pions and kaons. While the knowledge of the primary cosmic ray spectrum below a few 100 GeV has improved considerably in the recent past [1], large uncertainties still exist in the primary energy range between 0.1 and 500 TeV responsible for the production of secondaries with momenta in the range under study here. Moreover, the details of high energy hadronic interactions still lack theoretical understanding and there is little experimental data in the relevant energy and phase space regions [2]. Therefore the ground-level muon flux and charge ratio are widely used to tune or verify the parameters of atmospheric cascade calculations [3–6]. Currently these calculations are of great interest, as they predict the absolute atmospheric neutrino fluxes [7] which are

needed to interpret the observed muon neutrino flux deficit [8–10] and to evaluate the backgrounds for neutrino astronomy.

The muon flux and charge ratio have been extensively studied with different experimental techniques [11]. However, results show discrepancies of about 10–20% with respect to each other, which exceed the uncertainties assigned to the individual measurements and thus indicate the presence of systematic effects not accounted for.

Here a new measurement of the atmospheric muon flux is presented using the precise muon spectrometer of the L3 detector located at the LEP collider at CERN, near Geneva, Switzerland. Special attention is given to the precise determination of all relevant detector and environmental parameters needed to convert the raw-data distributions into an absolute surface level flux. The large statistics available permits extensive studies of the residual systematic uncertainties.

2. Experimental setup

The momentum distribution of atmospheric muons is measured with the upgraded L3 setup of the L3 detector [12] known as L3 + C [13]. The parts of the detector used in this analysis are sketched in Fig. 1. After passing through the stratified rock overburden, called "molasse", the arrival time t_0 of a muon is measured with a resolution of 1.7 ns by a 202 m^2 scintillator array placed on top of the L3 detector. The array is composed of 34 modules, each read out by two photomultipliers in coincidence to reduce noise. Inside a volume of about 1000 m^3 with a magnetic field of 0.5 T, the coordinates and slopes of a muon track are measured in up to six drift chambers in the bending plane and up to eight times in the non-bending plane. These chambers are arranged concentrically around the LEP beam line in two groups of eight octants, each containing three layers of drift cells. By subtracting the
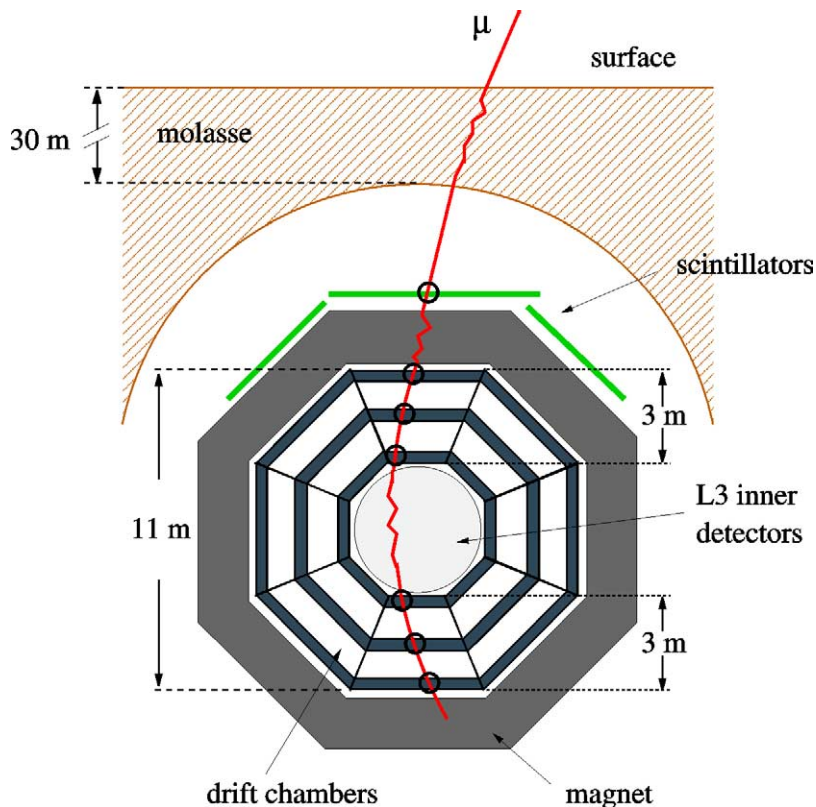

Fig. 1. Schematic view of the experimental setup.

t_0 time from the arrival times of the drift electrons at the sense wires, a track position in each chamber can be reconstructed with a precision of about 60 μm in the bending plane and 1 mm in the non-bending plane.

Only three points are needed to determine the radius of the track in the magnetic field, therefore the momentum of a muon traversing two octants can be measured twice. This redundancy is used to evaluate the detector efficiencies and the resolution of the apparatus. The best resolution is obtained when fitting the six points together over the full track length of 11 meters. The multiple scattering and energy loss inside the L3 inner detectors, as well as the effect of the inhomogeneous magnetic field are taken into account using the procedure proposed in Ref. [14].

Equipped with a trigger and data acquisition system independent of the normal L3 data-taking, $L3 + C$ recorded 1.2×10^{10} atmospheric muon triggers during its operation in the years 1999 and 2000.

The $L3 + C$ experiment was located 450 m above sea level at a longitude of $6.02° E$ and a latitude of $46.25° N$.

For vertically incident muons, the mean energy loss in the molasse ($X = 6854$ g cm^{-2}) and the magnet ($X = 1227$ g cm^{-2}) is 19 GeV at low momenta and reaches 57 GeV at 1 TeV.

3. Analysis

3.1. Detector and molasse simulation

The geometrical acceptance of the $L3 + C$ detector and the stochastic energy loss in the molasse overburden are evaluated using the following simulation procedure: Monte Carlo events are generated on the surface using a parameterization of the zenith angle and momentum dependence of the muon spectrum as obtained with the CORSIKA [15] program. These simulated muons are then tracked through a GEANT [16,17] model of the $L3 + C$ environment which includes the molasse, access shafts and the concrete structures around the cavern which hosts the apparatus. Finally, the detector response is simulated with a detailed GEANT description of the L3 detector. The generated detector signals are reconstructed with the same program used for the data. In total 1.7×10^9 re-constructed Monte Carlo events are used in this analysis.

3.2. Event selection

The data analysis is restricted to events with three position measurements in at least one octant, a scintillator hit and good running conditions during data-taking. A total of 1.2×10^9 reconstructed muon tracks are retained.

The shielding of the 30 m of molasse overburden absorbs most of the charged air-shower particles other than muons. The number of muons produced in e^+e^- collisions by LEP is negligible compared to the flux of atmospheric muons. Therefore no background rejection is needed. The data selection focuses on two topics. Firstly, fiducial volume cuts are defined to assure a good description of the data by the simulation. Secondly, selection cuts are imposed on the track quality to enhance the momentum and angular resolution. These selection criteria are:

- The muon track positions must be measured in six layers in the bending plane.
- The momentum resolution, calculated from the quality of the track position measurements, should not exceed its nominal value by more than 50%.
- At least four position measurements (two in each octant) should be present in the non-bending plane.
- The χ^2 of a fit of the tracks to a circle within an octant must satisfy $\chi^2/\text{ndf} < 4$.
- The difference between the two photomultiplier time measurements from the same scintillator module must be below 8 ns.

After these cuts, 2×10^7 data events remain for the muon spectrum analysis. The selection efficiencies depend on the charge, momentum and direction of the muon. For muons with momenta above 80 GeV, the average efficiency is 7.6% for the fiducial volume cut and 33.3% for the quality selection.

4% of the raw events are multi-muon events. Each individual muon is counted as an input to the spectrum data.
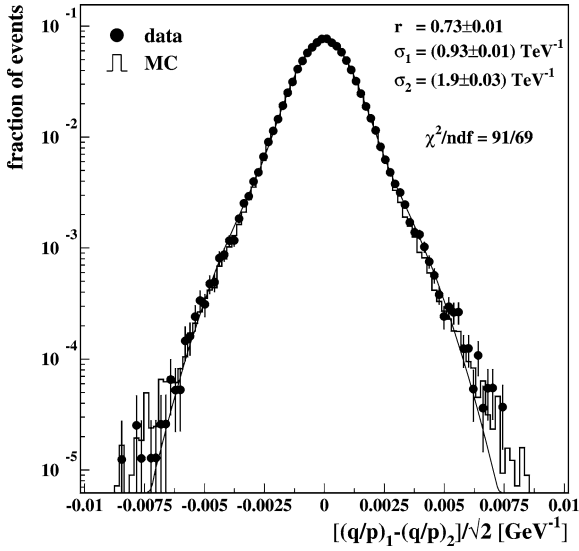
Fig. 2. Curvature difference at 100 GeV. The line denotes a fit with a sum of two Gaussian distributions with width σ_1 and σ_2. The fraction of events with width σ_1 is denoted by r.

3.3. Momentum resolution

The single-octant resolution is inferred directly from the data by comparing the two independent curvature measurements of muons traversing two octants. An example of the curvature difference is shown in Fig. 2. These measurements are used to tune the detector simulation, from which the resolution of the full fit is determined. The relative momentum resolution $\Delta p/p$ as a function of momentum at the detector-level is shown in Fig. 3(a). The maximum detectable momentum of the spectrometer, defined as the momentum at which $\Delta p/p$ reaches unity, is 0.78 TeV for muons measured in only one octant and about 5 TeV for muons measured in two octants.

3.4. Detector efficiencies

The efficiency of each subdetector is studied by exploiting redundancies in the measurement process. For about 50% of the tracks, the muon arrival time is also deduced from the muon chambers. These tracks are used to determine the scintillator efficiencies as a function of time and position on the array. A mean efficiency of 95.6% is found at the start of data-taking decreasing continuously to 94.5% towards the end of
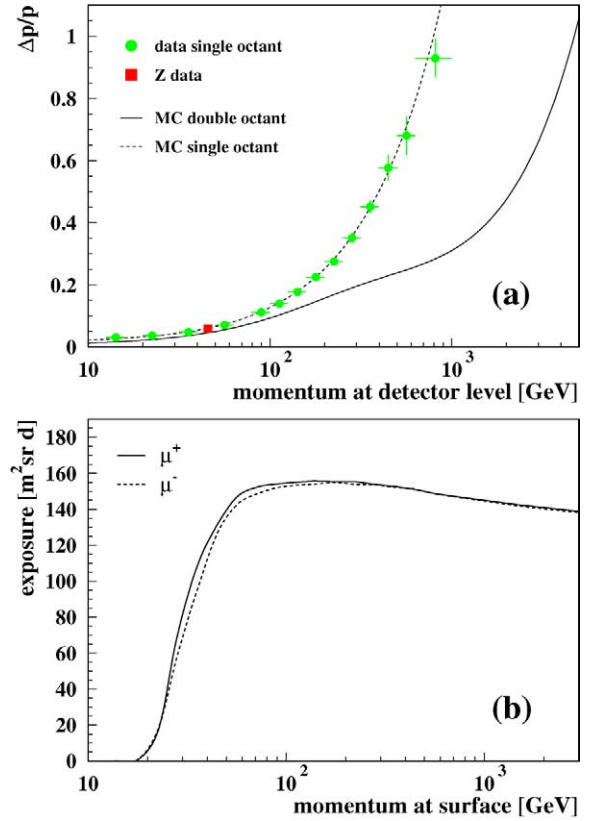
Fig. 3. L3 + C detector performance: (a) relative momentum resolution as a function of the muon momentum at the detector-level, (b) detector exposure for this analysis as a function of the muon momentum at surface for positive and negative muons (the sum over all zenith angle bins is shown).

2000. The possibility of reconstructing a muon within a single octant is used to scan the drift-layer performance of the facing octant. On average, a fraction of 10.5% of the drift cells are found to have an efficiency lower than 80%. These regions are excluded in both the data and Monte Carlo reconstruction. Under these conditions the trigger efficiency is determined from redundant trigger classes to be 99.85% on average.

During data-taking, the total effective running time was continuously measured with a 10 MHz live-time counter, which is disabled whenever the trigger system is not ready to accept new data. In addition, each second an external trigger signal was sent to the L3 + C trigger system. The number of these external triggers on tape compared to the total number of running sec-

onds gives another estimate of the effective running time and agrees with the value from the live-time counter within 0.02%.

3.5. Selection efficiency

Using the possibility to measure a muon independently in two detector parts, the selection efficiencies are determined in the following way: the detector is subdivided into two hemispheres, i and j, and the conditional hemisphere selection probabilities ε_i are measured for data and Monte Carlo separately as a function of the muon charge q, momentum p and zenith angle θ. In the absence of correlated inefficiencies, the total selection efficiency for accepting a track in the two hemispheres is given by the product $\varepsilon_1 \times \varepsilon_2$. The ratio

$$r = \frac{(\varepsilon_1 \times \varepsilon_2)^{\text{data}}}{(\varepsilon_1 \times \varepsilon_2)^{\text{MC}}} \tag{1}$$

is used to correct the differences between data and Monte Carlo. Depending on the zenith angle range and the data-taking year, r varies from 0.84 to 0.90. A large fraction of this correction factor originates from a defect in the TDCs used to read out the muon chambers, giving rise to an 8% inefficiency for the full track selection.

3.6. Surface spectrum

The relation between the momentum distribution measured in L3 + C and the muon surface spectrum is given by

$$\mathbf{n} = \tau \cdot \mathbf{E} \cdot \mathbf{R} \cdot \mathbf{A} \cdot \mathbf{m}. \tag{2}$$

Here $\mathbf{n}$ is the vector of events n_i with measured momenta between $[qp_i, qp_{i+1}]$. The effective live-time is given by τ and $\mathbf{R}$ denotes the migration matrix, i.e., the conditional probability of measuring a momentum qp_i given a surface momentum qp_j. $\mathbf{A}$ is the diagonal matrix of geometrical acceptances as a function of the surface momentum and $\mathbf{E}$ is the diagonal matrix of detector efficiencies as a function of momentum at the detector-level. The vector $\mathbf{m}$ contains the true surface spectrum integrated over a surface momentum bin. The complete detector matrix, $\mathbf{D} \equiv \mathbf{E} \cdot \mathbf{R} \cdot \mathbf{A}$, is evaluated from the measured detector efficiencies and the detector simulation as follows:

$$D_{ij} = \varepsilon_i r_i S_{\text{MC}} \left(\frac{n_{ij}^{\text{sel}}}{N_j^{\text{gen}}} \right)_{\text{MC}} \Delta\Omega, \tag{3}$$

where S_{MC} is the surface area used in the Monte Carlo generator, $\Delta\Omega$ the solid angle of the zenith bin under study, ε_i includes the scintillator and trigger efficiencies and r_i is the selection efficiency correction discussed above. n_{ij}^{sel} denotes the number of selected Monte Carlo events found within a detector-level momentum bin i, which were generated within the momentum bin j at the surface, and N_j^{gen} is the total number of Monte Carlo events generated within this surface momentum bin.

The effective acceptance of this analysis is calculated by summing over the columns of the detector matrix, which yields the geometrical factor for a muon being registered in the detector and fulfilling the selection cuts. The product of the effective acceptance and the live-time gives the total exposure, shown in Fig. 3(b) for positive and negative muons as a function of surface momentum. It rapidly decreases at low energies due to the momentum cut-off caused by the molasse overburden. Below 200 GeV, positive and negative muons have different acceptances, because the magnetic field bends their tracks in opposite directions and correspondingly into different detector regions. At large momenta the acceptance decreases with the performance of the full detector fit and a more difficult reconstruction caused by the increasing production of delta rays.

The measurement Eq. (2) is solved using the least squares method, by minimizing

$$\chi^2 = \sum_i \frac{(n_i - \tau \sum_j D_{ij} m_j)^2}{\sigma_i(\mathbf{m})^2}, \tag{4}$$

where σ_i contains the statistical errors of the data and the detector matrix:

$$\sigma_i = \sqrt{n_i + \tau^2 \sum_j V[D_{ij}] m_j^2}. \tag{5}$$

In the first step, the statistical Monte Carlo variances $V[D_{ij}]$ are set to zero, such that Eq. (4) becomes linear with respect to the surface spectrum $\mathbf{m}$ and its solution is

$$\hat{\mathbf{m}} = \frac{1}{\tau} (\mathbf{D}^{\mathsf{T}} \mathbf{W} \mathbf{D})^{-1} \mathbf{D}^{\mathsf{T}} \mathbf{W} \mathbf{n} \tag{6}$$

with covariance matrix

$$\mathbf{V}[\hat{\mathbf{m}}] = \left(\mathbf{D}^{\mathrm{T}}\mathbf{W}\mathbf{D}\right)^{-1}. \tag{7}$$

Here $\mathbf{W}$ denotes the diagonal weight matrix containing the statistical errors of the data and the Monte Carlo, $W_{ii} = 1/\sigma_i^2$.

The minimization of Eq. (4) is then repeated using the solution $\hat{\mathbf{m}}$ of the previous iteration for the calculation of the errors in Eq. (5). This process is repeated until the maximum relative difference to the result of the previous iteration is below 10^{-6}. Typically four iterations are needed.

4. Systematic uncertainties

4.1. Normalization uncertainties

Uncertainties on the live-time and the trigger and scintillator efficiencies give rise to a normalization uncertainty of 0.7%.

The uncertainty of the detector acceptance is assessed in three studies: first, the results obtained for statistically independent data subsamples, as, for instance, the data collected in 1999 and 2000 or in different detector parts, are compared. Second, the muon flux and charge ratio are measured as a function of the azimuthal angle. At large momenta, geomagnetic effects and the variation of the molasse overburden are not important, and therefore a flat distribution is expected. Finally, the stability of the measured flux and charge ratio with respect to a variation of the selection criteria is investigated.

From these studies, additional normalization uncertainties in the absolute muon flux are derived. These range from 1.7% to 3.7% depending on the zenith angle. For the charge ratio normalization uncertainties between 1.0% and 2.3% are estimated.

Fig. 4 shows an example of the stability of the measured muon flux within the two data-taking years for zenith angles between 0 and 32 degrees. Since the muon production is known to change with atmospheric conditions [18,19], the observed variation of the muon flux is compared to an air-shower simulation with the TARGET [20] program using atmospheric density profiles measured in balloon flights close to the experiment [21]. Good overall agreement between data and
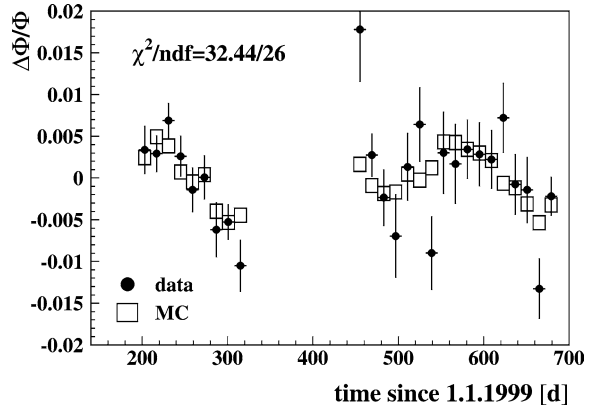

Fig. 4. Relative rate change with time for muon momenta between 50 and 62 GeV, compared to a prediction of the atmospheric effect obtained with the TARGET air-shower simulation. The value of a χ^2 comparison of data and Monte Carlo is also shown.

Monte Carlo is observed. However, the full comparison to the rates in 26 weeks and 14 momentum bins yields a χ^2/ndf of 526/364. The assumption that this large value is caused by detector inefficiencies not accounted for, leads to an additional normalization uncertainty of 0.3%, which is well within the above estimated uncertainties.

4.2. Momentum scale uncertainties

Due to the steepness of the muon spectrum, even small uncertainties in the absolute momentum scale can introduce a considerable bias in the muon flux measurement.

The uncertainty on the L3 magnetic field strength introduces a momentum scale bias of less than 0.4% [22].

Furthermore, the momentum measurement is subject to uncertainties of the detector alignment. A systematic shift of the chamber positions may introduce a constant offset C. The measurement of the curvature, q/p, and the alignment related momentum scale uncertainty, δ_{al} is given by

$$\delta_{\mathrm{al}} = \frac{\Delta C}{q/p + \Delta C}p, \tag{8}$$

and depends on the muon charge. Within one octant, the alignment is measured by an optical alignment system [23] with a precision corresponding to 0.19 TeV^{-1} [24]. The relative alignment of the muon chamber oc-

tants, relevant for this analysis, is determined from the data itself with a precision between 0.075 and 0.152 TeV^{-1} [25], depending on the zenith angle.

The uncertainty due the molasse overburden affects the conversion of the measured flux at the detector to the surface. The results of two survey drillings at different locations close to L3 + C provide an absolute measurement of the L3 + C matter overburden. The influence of molasse inhomogeneities and of surface installations not included in the L3 + C simulation is estimated by studying the variance of the muon flux as a function of the azimuthal angle near the momentum threshold. This leads to an uncertainty of the average rock density of 2%, which is equivalent to an energy loss uncertainty of 0.4 GeV in the vertical direction.

Good agreement between the muon energy-loss calculation used here [16,17] and other approaches [26–28] is found. The residual differences correspond to a momentum scale uncertainty below or less than 0.3% in the vertical direction.

The relative momentum scale uncertainties for vertically incident muons are displayed in Fig. 5(a). At low energies the molasse uncertainty contributes the most, whereas above 100 GeV the alignment uncertainties dominate.

4.3. Detector matrix uncertainty

The limited Monte Carlo statistics affects the precision of the detector matrix **D**. Below 200 GeV, it dominates the total statistical uncertainty in the denominator of Eq. (4), contributing about 0.5% to the total uncertainty per zenith angle bin.

In order to estimate the influence of the uncertainty of the momentum resolution on the measured muon flux, the minimization of Eq. (4) is repeated with different detector matrices, for which the momentum resolution is altered by ±8%. This corresponds to the estimated uncertainty of its Monte Carlo prediction. As expected, no differences are found at low momenta. Above 200 GeV, the observed relative flux change Δ_Φ is well described by

$$\Delta_\Phi = c \cdot (p - 0.2 \text{ TeV}) \tag{9}$$

with $c = 0.03$ TeV^{-1}. The observed difference between the high-energy muon flux measured in different detector regions leads to a somewhat larger value of $c = 0.06$ TeV^{-1}.

4.4. Total uncertainty

The total uncertainties of the muon flux and charge ratio are obtained by adding the individual contributions in quadrature. The different sources of the vertical uncertainties are shown in Fig. 5(b) and (c). The muon flux uncertainty is dominated by the uncertainty of the molasse overburden at low momenta and by the alignment and resolution uncertainty at high momenta. The minimal uncertainty is 2.3% at 150 GeV in the vertical direction. The vertical charge ratio uncertainty is below 2% up to momenta of 100 GeV. Above this momentum, it rises rapidly with the alignment uncertainties.

These uncertainties are fully correlated between different momenta for a given zenith angle bin. As approximately the same detector parts are used to measure the muons in neighboring zenith angles, the systematic uncertainties are also correlated with respect to the zenith angle. The estimated correlation coefficients are listed in Table 1.

4.5. Z-events

The understanding of the detector is validated by analyzing the muons produced at LEP via the process

$$e^+e^- \to Z \to \mu^+\mu^-,$$

recorded during the LEP calibration runs at a mean centre-of-mass energy of 91.27 GeV. The selection criteria include the requirement of a muon track close to the collision point and an event-time in coincidence with the LEP beam crossing time. The number of selected muons with a momentum above 60% of the beam energy is converted to an absolute cross section resulting in

$$\sigma^{\text{L3+C}}_{\mu^+\mu^-} = 1.447 \pm 0.071(\text{stat.}) \pm 0.021(\text{syst.}) \text{ nb.} \tag{10}$$

Here the quoted systematic uncertainty includes only sources which are not relevant to the muon spectrum measurement, such as the luminosity.

Using the LEP precision measurements [29], the Standard Model expectation of $\sigma_{\mu^+\mu^-}$ is calculated [30] to be

$$\sigma^{\text{SM}}_{\mu^+\mu^-} = 1.4840 \pm 0.0013 \text{ nb}, \tag{11}$$
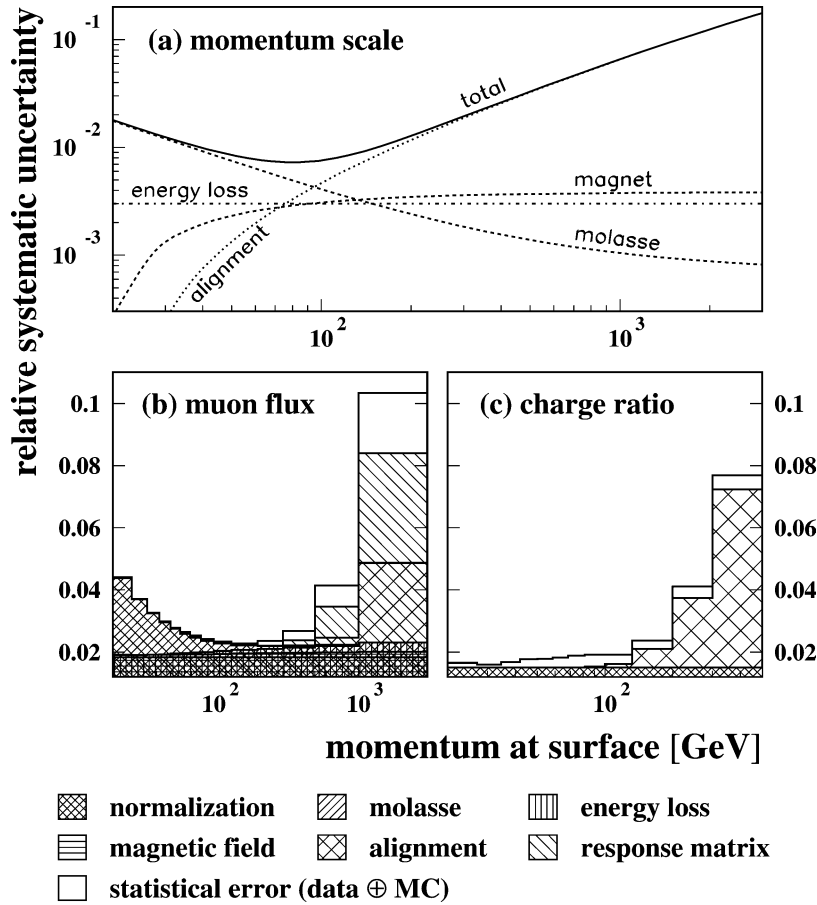
Fig. 5. Relative uncertainties of the vertical zenith angle bin measurements for (a) the momentum scale, (b) the muon flux and (c) the charge ratio. The individual contributions are added in quadrature.

Table 1
Correlation coefficients of the detector-related systematic uncertainties between different zenith angle bins from 0° to 58°

$\cos\theta$	0.525–0.600	0.600–0.675	0.675–0.750	0.750–0.825	0.825–0.900	0.900–0.938	0.938–0.975	0.975–1.000
0.525–0.600	1.00	0.91	0.99	0.94	0.93	0.00	0.00	0.00
0.600–0.675	0.91	1.00	0.96	0.76	0.88	0.00	0.00	0.00
0.675–0.750	0.99	0.96	1.00	0.91	0.95	0.00	0.00	0.00
0.750–0.825	0.94	0.76	0.91	1.00	0.93	0.00	0.00	0.00
0.825–0.900	0.93	0.88	0.95	0.93	1.00	0.01	0.01	0.01
0.900–0.938	0.00	0.00	0.00	0.00	0.01	1.00	1.00	1.00
0.938–0.975	0.00	0.00	0.00	0.00	0.01	1.00	1.00	1.00
0.975–1.000	0.00	0.00	0.00	0.00	0.01	1.00	1.00	1.00

which is in excellent agreement to the value measured here.

Thus this study verifies the L3 + C acceptance calculation and a normalization uncertainty of < 5.2%

Table 2

Muon flux, Φ, multiplied with the third power of the momentum, and charge ratio for $0.975 < \cos\theta < 1.000$. The statistical, Δ^{stat}, and the systematical, Δ^{syst}, uncertainties are given. ρ_Φ and ρ_R are the statistical correlation coefficients between neighboring momentum bins, as derived from Eq. (7)

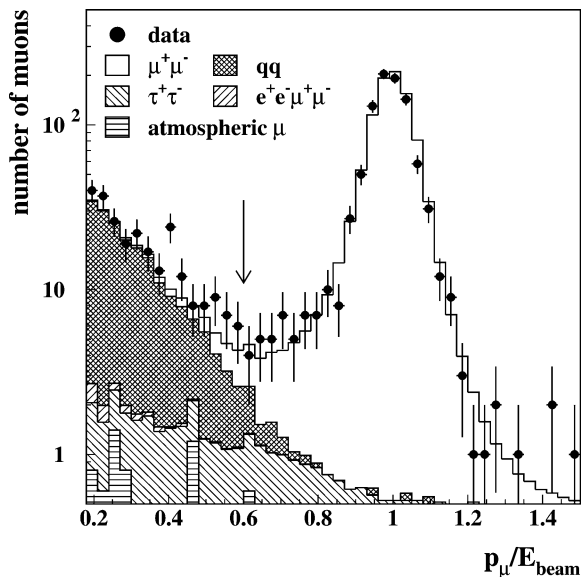| Momentum interval [GeV]	$\langle p \rangle$ [GeV]	$\Phi \cdot \langle p \rangle^3$ $\left[\frac{\text{GeV}^2}{\text{cm}^2\,\text{s}\,\text{sr}}\right]$	$\Delta^{\text{stat}}_\Phi$ [%]	ρ_Φ	$\Delta^{\text{syst}}_\Phi$ [%]	R	Δ^{stat}_R [%]	ρ_R	Δ^{syst}_R [%]
20.0–27.0	23.18	0.217	0.4		4.4	1.274	0.7		1.5
27.0–34.5	30.47	0.231	0.3	-0.24	3.7	1.284	0.6	-0.24	1.5
34.5–42.0	38.02	0.244	0.4	-0.22	3.3	1.295	0.8	-0.22	1.5
42.0–50.0	45.78	0.252	0.5	-0.24	3.0	1.269	0.9	-0.24	1.5
50.0–58.5	54.04	0.257	0.5	-0.26	2.8	1.286	1.0	-0.26	1.5
58.5–68.5	63.25	0.261	0.5	-0.31	2.6	1.298	1.0	-0.31	1.5
68.5–81.5	74.63	0.266	0.5	-0.31	2.5	1.273	1.1	-0.31	1.5
81.5–100	90.13	0.262	0.6	-0.30	2.4	1.293	1.2	-0.29	1.5
100–132	114.5	0.264	0.5	-0.26	2.3	1.286	1.0	-0.26	1.6
132–200	161.3	0.250	0.5	-0.22	2.2	1.287	1.1	-0.21	2.1
200–300	243.0	0.233	0.8	-0.22	2.2	1.327	1.7	-0.22	3.7
300–500	381.9	0.203	1.2	-0.27	2.4	1.276	2.6	-0.27	7.2
500–1000	687.2	0.151	2.3	-0.28	3.5				
1000–3000	1599	0.087	6.0	-0.30	8.4				

Fig. 6. Momentum distribution of the selected Z-events and the background. The Monte Carlo [31–33] events are normalized to the Standard Model expectation as given in Eq. (11). The arrow indicates the low momentum cut.

at 68% C.L. can be stated. Although this number is larger than the estimated systematic uncertainty of the muon flux normalization, it provides an absolute systematic cross-check qualitatively different from the relative studies described above.

The momentum distribution of the selected events, displayed in Fig. 6, shows good agreement between the data and the simulation. From the peak position of the data, an absolute momentum scale uncertainty of < 370 MeV and a single octant alignment uncertainty of < 0.1 TeV^{-1} is derived.

As can be seen in figure Fig. 3(a), the momentum resolution derived from the Z muon sample agrees well with the one measured with atmospheric muons.

5. Results

The muon fluxes, Φ, conventionally multiplied by the third power of the momentum, and the charge ratios, R, are listed for each zenith angle bin in Tables 2–9 with their statistical and systematic uncertainties. The statistical correlation coefficients, ρ, between neighboring momentum bins, as derived from Eq. (7), are also given. Due to the limited detector resolution these correlations are inevitable. However, the momentum binning is chosen such that only neighboring bins have a significant correlation.

Table 3
Muon flux and charge ratio for $0.938 < \cos\theta < 0.975$

Momentum interval [GeV]	$\langle p \rangle$ [GeV]	$\Phi \cdot \langle p \rangle^3$ $\left[\frac{\mathrm{GeV}^2}{\mathrm{cm}^2\,\mathrm{s}\,\mathrm{sr}}\right]$	$\Delta_\Phi^{\mathrm{stat}}$ [%]	ρ_Φ	$\Delta_\Phi^{\mathrm{syst}}$ [%]	R	Δ_R^{stat} [%]	ρ_R	Δ_R^{syst} [%]
27.0–34.5	30.47	0.237	0.3		4.5	1.265	0.6		2.3
34.5–42.0	38.02	0.254	0.4	−0.23	4.1	1.261	0.8	−0.22	2.3
42.0–50.0	45.78	0.259	0.5	−0.24	3.8	1.265	1.0	−0.24	2.3
50.0–58.5	54.04	0.264	0.5	−0.26	3.7	1.297	1.1	−0.26	2.3
58.5–68.5	63.25	0.266	0.6	−0.30	3.5	1.250	1.1	−0.30	2.3
68.5–81.5	74.63	0.270	0.6	−0.31	3.4	1.319	1.2	−0.31	2.3
81.5–100	90.13	0.271	0.6	−0.29	3.3	1.259	1.3	−0.29	2.3
100–132	114.5	0.270	0.5	−0.25	3.2	1.296	1.1	−0.25	2.5
132–200	161.3	0.262	0.6	−0.21	3.1	1.281	1.2	−0.21	3.0
200–300	243.0	0.241	0.9	−0.21	3.1	1.273	1.8	−0.21	4.8
300–500	382.1	0.219	1.3	−0.27	3.2	1.389	2.7	−0.27	8.3
500–1000	687.8	0.165	2.4	−0.27	4.2				
1000–3000	1604	0.093	6.5	−0.30	9.2				

Table 4
Muon flux and charge ratio for $0.900 < \cos\theta < 0.938$

Momentum interval [GeV]	$\langle p \rangle$ [GeV]	$\Phi \cdot \langle p \rangle^3$ $\left[\frac{\mathrm{GeV}^2}{\mathrm{cm}^2\,\mathrm{s}\,\mathrm{sr}}\right]$	$\Delta_\Phi^{\mathrm{stat}}$ [%]	ρ_Φ	$\Delta_\Phi^{\mathrm{syst}}$ [%]	R	Δ_R^{stat} [%]	ρ_R	Δ_R^{syst} [%]
27.0–34.5	30.47	0.245	0.4		4.3	1.265	0.7		2.3
34.5–42.0	38.02	0.257	0.4	−0.24	3.9	1.296	0.9	−0.24	2.3
42.0–50.0	45.78	0.265	0.5	−0.26	3.6	1.302	1.1	−0.26	2.3
50.0–58.5	54.04	0.273	0.5	−0.28	3.4	1.267	1.1	−0.28	2.3
58.5–68.5	63.25	0.279	0.5	−0.31	3.2	1.287	1.1	−0.31	2.3
68.5–81.5	74.64	0.282	0.5	−0.31	3.1	1.272	1.1	−0.30	2.3
81.5–100	90.14	0.283	0.5	−0.27	3.0	1.288	1.1	−0.27	2.4
100–132	114.5	0.284	0.5	−0.23	2.9	1.303	0.9	−0.23	2.6
132–200	161.3	0.274	0.5	−0.19	2.8	1.325	1.0	−0.19	3.8
200–300	243.0	0.255	0.7	−0.19	2.8	1.300	1.4	−0.19	6.8
300–500	382.0	0.220	1.1	−0.23	2.9	1.437	2.2	−0.23	12.0
500–1000	687.3	0.172	1.9	−0.25	4.2				
1000–3000	1599	0.091	5.7	−0.29	11.3				

The average momenta, $\langle p \rangle$, within a momentum range $[p_1, p_2]$ are calculated [34] by fitting the phenomenological muon flux function from Ref. [11] to our data and solving

$$\Phi(\langle p \rangle) = \frac{1}{p_2 - p_1} \int\limits_{p_1}^{p_2} \Phi(p)\, dp. \tag{12}$$

It should be noted that the fluxes are neither corrected for the altitude of L3 + C nor for the atmospheric profile to avoid additional theoretical uncertainties. Instead, we quote the average atmospheric mass overburden X above L3 + C, which was continuously measured with balloon flights from close to the experiment to altitudes of over 30 km [21]. The parameterization of Ref. [35] is used to describe the mass profile X in $\mathrm{g\,cm}^{-2}$ as a function of the altitude h in

Table 5
Muon flux and charge ratio for $0.825 < \cos\theta < 0.900$

Momentum interval [GeV]	$\langle p \rangle$ [GeV]	$\Phi \cdot \langle p \rangle^3$ $\left[\frac{\text{GeV}^2}{\text{cm}^2\,\text{s}\,\text{sr}}\right]$	$\Delta_\Phi^{\text{stat}}$ [%]	ρ_Φ	$\Delta_\Phi^{\text{syst}}$ [%]	R	Δ_R^{stat} [%]	ρ_R	Δ_R^{syst} [%]
34.5–42.0	38.02	0.263	0.4		3.9	1.248	0.8		1.3
42.0–50.0	45.78	0.269	0.5	−0.28	3.5	1.288	1.1	−0.28	1.3
50.0–58.5	54.04	0.274	0.5	−0.29	3.3	1.280	1.1	−0.29	1.3
58.5–68.5	63.25	0.284	0.6	−0.32	3.1	1.285	1.2	−0.32	1.3
68.5–81.5	74.64	0.280	0.6	−0.31	2.9	1.274	1.2	−0.31	1.3
81.5–100	90.14	0.288	0.6	−0.28	2.8	1.302	1.3	−0.28	1.3
100–132	114.5	0.290	0.5	−0.24	2.6	1.280	1.1	−0.24	1.4
132–200	161.3	0.279	0.6	−0.20	2.6	1.313	1.1	−0.20	2.0
200–300	243.1	0.264	0.8	−0.20	2.5	1.301	1.7	−0.20	4.7
300–500	382.1	0.232	1.3	−0.27	2.6	1.318	2.6	−0.27	11.3
500–1000	686.8	0.167	2.5	−0.30	4.2				
1000–3000	1587	0.087	7.9	−0.37	10.4				

Table 6
Muon flux and charge ratio for $0.750 < \cos\theta < 0.825$

Momentum interval [GeV]	$\langle p \rangle$ [GeV]	$\Phi \cdot \langle p \rangle^3$ $\left[\frac{\text{GeV}^2}{\text{cm}^2\,\text{s}\,\text{sr}}\right]$	$\Delta_\Phi^{\text{stat}}$ [%]	ρ_Φ	$\Delta_\Phi^{\text{syst}}$ [%]	R	Δ_R^{stat} [%]	ρ_R	Δ_R^{syst} [%]
34.5–42.0	38.02	0.255	0.5		4.6	1.279	1.0		1.0
42.0–50.0	45.78	0.265	0.5	−0.32	4.2	1.284	1.1	−0.32	1.0
50.0–58.5	54.04	0.275	0.6	−0.32	3.9	1.263	1.1	−0.32	1.0
58.5–68.5	63.25	0.283	0.6	−0.35	3.7	1.261	1.2	−0.35	1.0
68.5–81.5	74.64	0.283	0.6	−0.33	3.6	1.271	1.2	−0.33	1.0
81.5–100	90.14	0.290	0.6	−0.29	3.4	1.281	1.2	−0.29	1.0
100–132	114.6	0.290	0.5	−0.26	3.3	1.256	1.0	−0.26	1.1
132–200	161.3	0.292	0.5	−0.20	3.2	1.280	1.1	−0.20	1.4
200–300	243.1	0.271	0.8	−0.22	3.2	1.297	1.6	−0.22	3.1
300–500	382.2	0.244	1.2	−0.28	3.3	1.428	2.5	−0.28	7.4
500–1000	687.5	0.191	2.2	−0.31	4.0				
1000–3000	1594	0.087	7.6	−0.36	8.4				

km above sea level:

$$X(h) = \begin{cases} A(h_b - h)^{(\alpha+1)}, & h \leqslant 11, \\ Be^{-\frac{h}{h_0}}, & h > 11. \end{cases} \quad (13)$$

A fit to the live-time weighted balloon data yields $A = 8.078 \times 10^{-5}$, $B = 1332$, $h_b = 39.17$, $h_0 = 6.370$ and $\alpha = 3.461$.

The measured muon fluxes at the L3 + C altitude are shown in Fig. 7 for each zenith angle bin. As no previous continuous zenith angle measurements exist in the large energy range examined here, only the ver-

tical flux can be compared to other experiments, as shown in Fig. 8. Only measurements providing an absolute normalization [36–44] are taken into account. The data are extrapolated to sea level using the muon flux predictions of the TARGET [20] program.

The comparison to low energy experiments [38–43] gives a good overall agreement with this analysis above about 40 GeV. At lower momenta, a systematic slope difference seems to be present, which corresponds to about three standard deviations of the systematic molasse uncertainty estimated above.

Table 7
Muon flux and charge ratio for $0.675 < \cos\theta < 0.750$

Momentum interval [GeV]	$\langle p \rangle$ [GeV]	$\Phi \cdot \langle p \rangle^3$ $\left[\frac{\text{GeV}^2}{\text{cm}^2\,\text{s}\,\text{sr}}\right]$	$\Delta_\Phi^{\text{stat}}$ [%]	ρ_Φ	$\Delta_\Phi^{\text{syst}}$ [%]	R	Δ_R^{stat} [%]	ρ_R	Δ_R^{syst} [%]
34.5–42.0	38.02	0.253	0.6	-0.38	4.6	1.273	1.2	-0.38	1.8
42.0–50.0	45.78	0.265	0.6	-0.35	4.1	1.292	1.1	-0.35	1.8
50.0–58.5	54.04	0.275	0.5	-0.38	3.7	1.263	1.1	-0.38	1.8
58.5–68.5	63.25	0.281	0.6	-0.34	3.4	1.273	1.2	-0.34	1.8
68.5–81.5	74.64	0.291	0.6	-0.31	3.1	1.263	1.2	-0.31	1.8
81.5–100	90.15	0.293	0.6	-0.27	2.9	1.260	1.2	-0.27	1.8
100–132	114.6	0.298	0.5	-0.22	2.7	1.266	1.0	-0.22	1.8
132–200	161.4	0.298	0.5	-0.23	2.5	1.281	1.0	-0.23	1.9
200–300	243.2	0.285	0.7	-0.29	2.4	1.267	1.6	-0.29	2.8
300–500	382.3	0.256	1.1	-0.31	2.6	1.394	2.5		5.7
500–1000	688.2	0.203	2.0	-0.35	3.5				
1000–3000	1601	0.120	5.3		7.8				

Table 8
Muon flux and charge ratio for $0.600 < \cos\theta < 0.675$

Momentum interval [GeV]	$\langle p \rangle$ [GeV]	$\Phi \cdot \langle p \rangle^3$ $\left[\frac{\text{GeV}^2}{\text{cm}^2\,\text{s}\,\text{sr}}\right]$	$\Delta_\Phi^{\text{stat}}$ [%]	ρ_Φ	$\Delta_\Phi^{\text{syst}}$ [%]	R	Δ_R^{stat} [%]	ρ_R	Δ_R^{syst} [%]
42.0–50.0	45.79	0.256	0.6	-0.41	4.7	1.262	1.3	-0.41	1.4
50.0–58.5	54.05	0.269	0.6	-0.42	4.3	1.284	1.2	-0.42	1.4
58.5–68.5	63.26	0.282	0.6	-0.36	4.0	1.261	1.3	-0.36	1.4
68.5–81.5	74.65	0.290	0.6	-0.31	3.7	1.277	1.3	-0.31	1.4
81.5–100	90.16	0.299	0.6	-0.26	3.5	1.267	1.2	-0.26	1.4
100–132	114.6	0.307	0.5	-0.22	3.3	1.287	1.0	-0.22	1.4
132–200	161.4	0.312	0.5	-0.24	3.1	1.274	1.0	-0.23	1.4
200–300	243.2	0.300	0.8	-0.32	3.0	1.278	1.6	-0.31	2.1
300–500	382.5	0.277	1.2	-0.35	3.1	1.317	2.4		4.7
500–1000	688.5	0.231	2.0	-0.38	3.8				
1000–3000	1602	0.117	6.3		8.7				

Only three previous experiments measured a normalized spectrum at high energies. The shape of the Kiel measurements [36] agree with this result over the full momentum range, but a lower flux normalization is determined by L3 + C.

The data obtained with the MARS apparatus [37] significantly disagree with this result, both in shape and normalization.

Above momenta of 50 GeV, the recent muon flux measurement from BESS-TeV [44] is in very good agreement with this result.

The measured charge ratios at the L3 + C altitude are shown in Fig. 9 for each zenith angle bin up to momenta of 500 GeV. In the considered momentum range, the charge ratio is independent of the momentum within the experimental uncertainties. The mean value in the vertical direction is found to be $1.285 \pm 0.003(\text{stat.}) \pm 0.019(\text{syst.})$ with a $\chi^2/\text{ndf} = 9.5/11$. This is in good agreement with the average of all previous measurements, $1.270 \pm 0.003(\text{stat.}) \pm 0.015(\text{syst.})$ [11]. It is worth noting, that the precision of the data of a single L3 + C zenith angle bin is comparable to

Table 9
Muon flux and charge ratio for $0.525 < \cos\theta < 0.600$

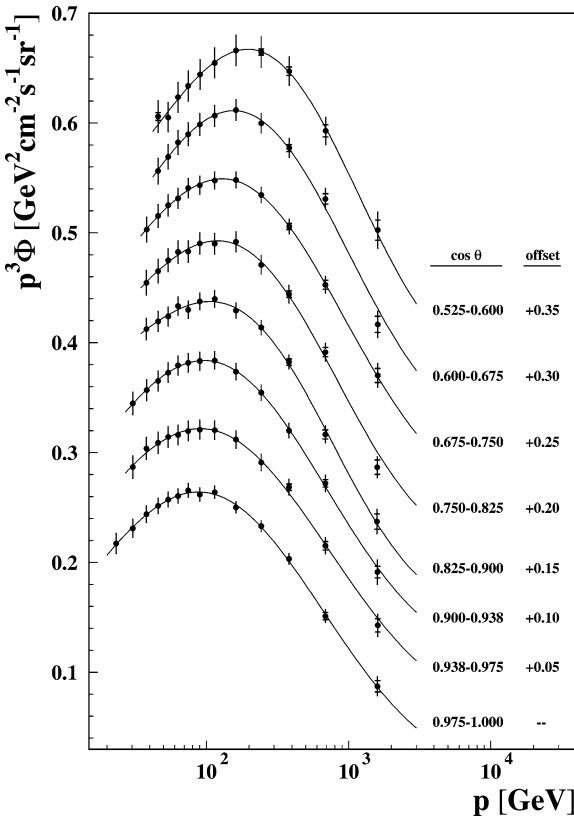| Momentum interval [GeV]	$\langle p \rangle$ [GeV]	$\Phi \cdot \langle p \rangle^3$ $\left[\frac{\text{GeV}^2}{\text{cm}^2\,\text{s}\,\text{sr}}\right]$	$\Delta^{\text{stat}}_{\Phi}$ [%]	ρ_{Φ}	$\Delta^{\text{syst}}_{\Phi}$ [%]	R	Δ^{stat}_{R} [%]	ρ_{R}	Δ^{syst}_{R} [%]
42.0–50.0	45.79	0.256	1.4		5.6	1.281	2.8		1.4
50.0–58.5	54.05	0.255	0.9	−0.49	5.3	1.269	1.7	−0.50	1.4
58.5–68.5	63.26	0.273	0.8	−0.45	5.1	1.290	1.6	−0.45	1.4
68.5–81.5	74.65	0.284	0.8	−0.38	4.9	1.280	1.5	−0.37	1.4
81.5–100	90.16	0.294	0.7	−0.32	4.7	1.278	1.4	−0.32	1.4
100–132	114.6	0.305	0.5	−0.25	4.6	1.258	1.1	−0.25	1.4
132–200	161.5	0.316	0.6	−0.22	4.5	1.254	1.2	−0.21	1.6
200–300	243.4	0.315	0.8	−0.22	4.4	1.285	1.7	−0.22	2.6
300–500	382.7	0.297	1.3	−0.30	4.4	1.332	2.6	−0.30	5.6
500–1000	689.3	0.243	2.3	−0.33	4.8				
1000–3000	1604	0.153	5.9	−0.36	9.4				

Fig. 7. The measured muon flux for zenith angles ranging from 0° (bottom) to 58° (top). The inner bars denote the statistical uncertainty, the full bars show the total uncertainty. For better visibility, an offset of 0.05 GeV^2 cm^{-2} s^{-1} sr^{-1} was added consecutively and lines are shown to guide the eye.
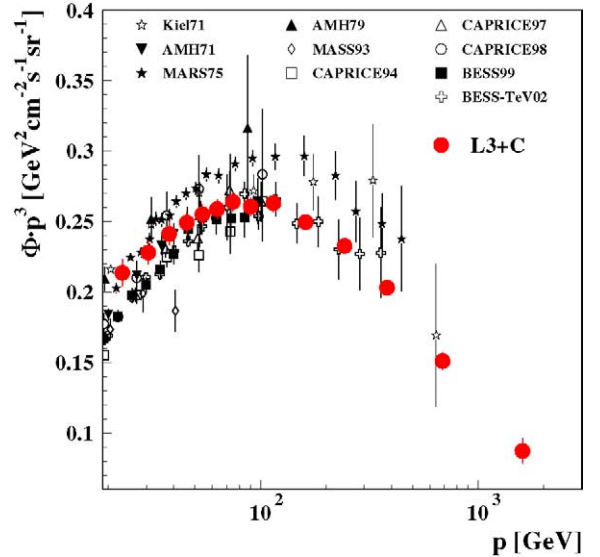

Fig. 8. The L3 + C vertical muon spectrum compared to previous direct measurements providing an absolute flux normalization. All data are extrapolated to sea level.

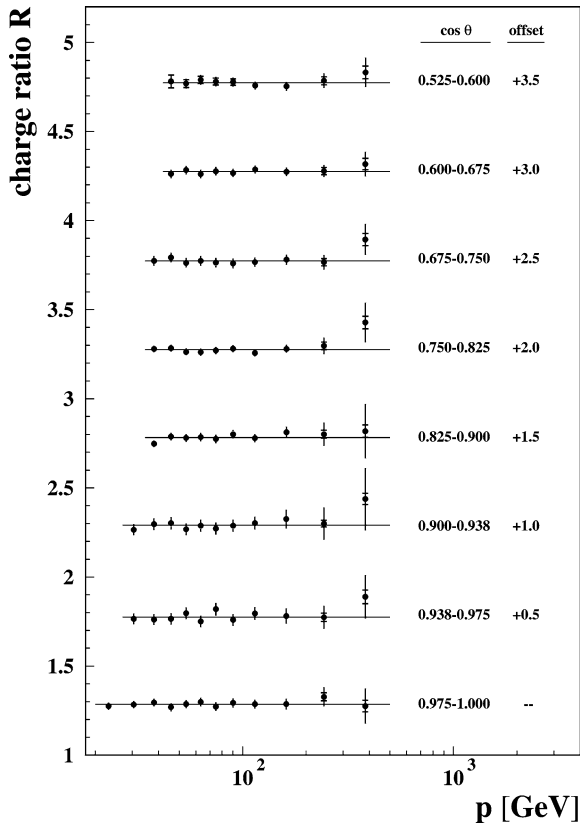the combined uncertainty of all data collected in the past.

Fig. 9. The measured muon charge ratio for zenith angles ranging from 0° (bottom) to 58° (top). The inner bars denote the statistical uncertainty, the full bars show the total uncertainty. For better visibility, an offset of 0.5 was added consecutively and lines are shown to guide the eye.

experiments. Those of us who are not from member states thank CERN for its hospitality and help. Furthermore, we would like to thank the Bartol group for providing the TARGET program.

References

[1] T.K. Gaisser, M. Honda, P. Lipari, T. Stanev, in: Proceedings of the 27th ICRC, Hamburg, 7–15 August, 2001, p. 1643, and references therein.
[2] R. Engel, T.K. Gaisser, T. Stanev, Phys. Lett. B 472 (2000) 113.
[3] M. Honda, T. Kajita, K. Kasahara, S. Midorikawa, Phys. Rev. D 52 (1995) 4985.
[4] V. Agrawal, T.K. Gaisser, P. Lipari, T. Stanev, Phys. Rev. D 53 (1996) 1314.
[5] E.V. Bugaev, et al., Phys. Rev. D 58 (1998) 054001.
[6] G. Fiorentini, V.A. Naumov, F.L. Villante, Phys. Lett. B 510 (2001) 173.
[7] T.K. Gaisser, M. Honda, Ann. Rev. Nucl. Part. Sci. 52 (2002) 153, and references therein.
[8] Super-Kamiokande Collaboration, Y. Fukuda, et al., Phys. Rev. Lett. 81 (1998) 1562.
[9] SOUDAN 2 Collaboration, W.W.M. Allison, et al., Phys. Lett. B 391 (1997) 491.
[10] MACRO Collaboration, M. Ambrosio, et al., Phys. Lett. B 434 (1998) 451.
[11] T. Hebbeker, C. Timmermans, Astropart. Phys. 18 (2002) 107.
[12] L3 Collaboration, B. Adeva, et al., Nucl. Instrum. Methods A 289 (1990) 35.
[13] L3 + C Collaboration, O. Adriani, et al., Nucl. Instrum. Methods A 488 (2002) 209.
[14] V. Innocente, E. Nagy, Nucl. Instrum. Methods A 324 (1993) 297.
[15] D. Heck, et al., CORSIKA: a Monte Carlo code to simulate extensive air showers, Forschungszentrum Karlsruhe, FZKA 6019, 1998.
[16] R. Brun, et al., GEANT 3, CERN Report DD/EE/84-1, 1987.
[17] S. Bottai, L. Perrone, Nucl. Instrum. Methods A 459 (2001) 319.
[18] P.H. Barrett, et al., Rev. Mod. Phys. 24 (1952) 133.
[19] S. Sagisaka, Nuovo Cimento C 9 (1986) 809.
[20] R. Engel, T.K. Gaisser, P. Lipari, T. Stanev, in: Proceedings of the 27th ICRC, Hamburg, 7–15 August, 2001, p. 1381.
[21] Service de Climatologie, Geneva.
[22] C. Brouwer, et al., Nucl. Instrum. Methods A 313 (1992) 50.
[23] P. Duinker, et al., Nucl. Instrum. Methods A 273 (1988) 814.
[24] M. Fabre, The dimuon mass resolution of the L3 experiment at LEP, Ph.D. thesis, ETH, Zürich, 1992.
[25] M. Unger, Measurement of the momentum spectrum of atmospheric muons with the L3 detector, Ph.D. thesis, Humboldt Universität Berlin, 2004, DESY-THESIS-2004-008.
[26] W. Lohmann, R. Kopp, R. Voss, Energy loss of muons in the energy range 1–10000 GeV, CERN Report 85-03, 1985.
[27] D.E. Groom, N.V. Mokhov, S.I. Striganov, At. Data Nucl. Data Tables 78 (2001) 183.
[28] D. Chirkin, W. Rhode, Muon Monte Carlo: A new high precision tool for muon propagation through matter, DESY-PROC-2002-01, 2002.
[29] Particle Data Group Collaboration, K. Hagiwara, et al., Phys. Rev. D 66 (2002) 010001, and references therein.
[30] D.Y. Bardin, et al., Comput. Phys. Commun. 133 (2001) 229.
[31] S. Jadach, B.F.L. Ward, Z. Was, Comput. Phys. Commun. 79 (1994) 503.
[32] T. Sjöstrand, Comput. Phys. Commun. 82 (1994) 74.
[33] J.A.M. Vermaseren, J. Smith, G. Grammer Jr., Phys. Rev. D 19 (1979) 137.
[34] G.D. Lafferty, T.R. Wyatt, Nucl. Instrum. Methods A 355 (1995) 541.
[35] K. Maeda, Fortschr. Phys. 21 (1973) 113.
[36] O.C. Allkofer, K. Carstensen, D.W. Dau, Phys. Lett. B 36 (1971) 425.
[37] C.A. Ayre, et al., J. Phys. G 1 (1975) 584.
[38] B.J. Bateman, et al., Phys. Lett. B 36 (1971) 144.

[39] P.J. Green, et al., Phys. Rev. D 20 (1979) 1598.

[40] M.P. De Pascale, et al., J. Geophys. Res. 98 (1993) 3501.

[41] CAPRICE Collaboration, J. Kremer, et al., Phys. Rev. Lett. 83 (1999) 4241.

[42] CAPRICE Collaboration, M. Boezio, et al., Phys. Rev. D 67 (2003) 072003.

[43] BESS Collaboration, T. Sanuki, et al., Phys. Lett. B 541 (2002) 234;
BESS Collaboration, T. Sanuki, et al., Phys. Lett. B 581 (2004) 272, Erratum.

[44] BESS Collaboration, S. Haino, et al., astro-ph/0403704.